Design and prototyping of the X-ray Fluorescence Spectrometer for online component analysis*

Guang-Zhi Li,[1] Chen Liu,[1,2,†] Tao Liu,[1] Shou-Yu Wang,[1,2] Xing-Chi Han,[3] Bing-Ying Xia,[1,2] and Zhi-Yang Liu[1]

[1]*Shandong Provincial Key Laboratory of Nuclear Science, Nuclear Energy Technology and Comprehensive Utilization, Weihai Frontier Innovation Institute of Nuclear Technology, School of Nuclear Science, Energy and Power Engineering, Shandong University, Shandong 250061, People's Republic of China*

[2]*WeiHai Research Institute of Industrial Technology of Shandong University, Weihai 264209, China*

[3]*Shandong Provincial Key Laboratory of Nuclear Science, Nuclear Energy Technology and Comprehensive Utilization, School of Nuclear Science, Energy and Power Engineering, Shandong University, Shandong 250061, People's Republic of China*

The X-ray fluorescence (XRF) system is designed and developed to enable faster and more convenient material composition detection and analysis. The system includes a Si-PIN detector, readout electronics, and a host computer. An algorithm is designed so that the detector can be used without vacuum and the device can achieve online composition analysis and data transmission. Testing was conducted using an iron ore sample, and the results demonstrate that the device achieves an energy resolution of 7.35% @6.4 keV. The measured result shows an 8% error compared to chemical methods. The device is capable of rapid composition analysis, with the potential for further applications in fields such as nuclear physics and mineral detection for industrial use.

Keywords: X-ray fluorescence (XRF), Si-PIN detector, readout electronics, elemental analysis, real-time measurement, non-destructive testing

I. INTRODUCTION

Since the discovery of X-rays by Wilhelm Conrad Röntgen [1] in 1895, their exceptional penetrability has led to widespread use in medical imaging. X-rays can pass through human body [2], creating images by measuring how much X-ray is absorbed or scattered [3], enabling non-invasive diagnostics. This ability to provide detailed internal images without surgery has revolutionized modern medicine. The discovery of X-rays also sparked a transformation in modern physics. Later, Max von Laue demonstrated that X-rays could diffract through crystals, a breakthrough that earned him the Nobel Prize in Physics [4]. Building on this, William and Lawrence Bragg extended Laue's theory and developed the principles of X-ray crystallography [5], laying the foundation for significant advancements in the study of atomic and molecular structures.

In 1913, Henry Moseley [6] discovered the relationship between the characteristic X-ray energy of elements and their atomic numbers and was the first to use X-rays for the purpose of composition analysis. These works played a crucial role in promoting atomic theory and enabling X-ray-based techniques to be used for elemental analysis. In 1923, Coster and Hevesy discovered the element Cr, which was the first element to be identified using X-ray spectral analysis [7, 8]. In 1928, Glocker and Schreiber [9] performed the first quantitative analysis of materials using X-ray fluorescence (XRF). It is an analytical technique based on the fluorescence generated by substances excited by X-rays. When the sample is irradiated with primary X-rays, the elements in the sample will be excited and emit characteristic X-rays with specific energies. By detecting the energies and intensities of these characteristic X-rays, the types and contents of the elements in the sample can be determined, thus realizing the qualitative and quantitative analysis of the material composition [6, 10]. In 1948, Herbert Friedman and Laverne Stanfield Birks developed the world's first commercial wavelength-dispersive X-ray fluorescence (WDXRF) spectrometer. In 1965, the introduction of the Si (Li) detector for detecting X-rays revolutionized the field. This detector was soon integrated into energy-dispersive X-ray fluorescence (EDXRF) spectrometers, becoming the core component in the X-ray detection area [11]. The development of XRF technology has been reviewed in Ref. [12–20].

With the advancement of X-ray detection technology, its applications have expanded to various fields, including geology [21, 22], archeology [23], medicine [24], bromatology [25], cultural heritage analysis [26], and nuclear physics experiments [27, 28]. Take nuclear physics experiment for example, the purity of the target material is a critical parameter that significantly impacts the experiment results associated with nuclear properties [29–32] and synthesizing new isotopes [33]. The application of X-rays in these diverse fields highlighted the potential of X-ray-based techniques for material analysis, which naturally led to the development of XRF. In the meanwhile, there still exist some challenges that have driven the continued enhancement of XRF technology, enabling more convenient and versatile applications across a wide range of scientific and industrial domains.

Up to now, XRF devices are primarily used in laborato-

---

* This work is partly supported by the National Natural Science Foundation of China (Grants No. 12225504, No. U2167202 and No. 12321005), and the Young Scholars Program of Shandong University, Weihai. The numerical calculations in this paper have been done on the super computing system in Shandong University, Weihai.

† Corresponding author, cliu@sdu.edu.cn

ries, requiring complex sample preparation and operation under vacuum conditions, which limits the measurement timeliness. In addition, the lack of an on-line transmission function also leads to inconvenience in the use process and makes them unsuitable for direct operation in complex environments like production lines. Therefore, an XRF device that enables faster measurement with online transmission and is more convenient to use has become an interesting research focus. Based on these issues, the current work has designed an XRF prototype, covering both hardware design and algorithm development. This system has overcome the limitations of traditional XRF devices to some extent, so as to conduct efficient elemental analysis in a wide range of practical applications.

In this paper, we describe the design and performance of the XRF system. Section 2 describes the design of the system. Sections 3, 4, 5 respectively cover the design of the hardware, the design of the software, the performance test results, and section 6 provides a summary.

II. DESIGN OF THE SYSTEM

The XRF is an elemental analysis device based on the principle of X-ray excitation fluorescence, primarily used for analyzing the composition of materials. Its physical foundation is based on Moseley's law [10] in atomic physics, which states that the energy of the characteristic X-rays emitted by an atom is proportional to the square of its atomic number. The concentration of the target element can be calculated from the intensity of the characteristic X-rays, enabling both qualitative and quantitative [34] analysis of the element. Figure 1 shows the full view of the device. The external dimensions of the device are 600 mm $\times$ 450 mm $\times$ 300 mm, with a total weight of 20 kg. The body is made of aluminum alloy, and it is equipped with 2 mm thick lead (Pb) as a shielding material to block excess radiation. The main parameters of the X-ray generator and detector are shown in Table 1 and Table 2.

The workflow diagram of the XRF system is presented in Fig. 2. As shown in Fig. 2, the working process of the XRF system begins with the X-ray generator, which generates primary X-rays under excitation from a high-voltage power supply. The sample is placed in a sample holder that can rotate at a constant speed, which helps eliminate the effects of uneven sample distribution.The X-rays pass through a collimator and then irradiate the sample to be tested. The sample is excited, producing characteristic X-rays. These characteristic X-rays are detected by a semiconductor detector. The signal is then amplified by a preamplifier and sent to readout electronics for processing. The results are transmitted to the host computer via a data interface for further processing, display, and analysis. Through this complete signal processing and transmission flow, the XRF system is able to perform both qualitative and quantitative analysis of the elements in the sample, providing an efficient and reliable technical means for material composition detection.

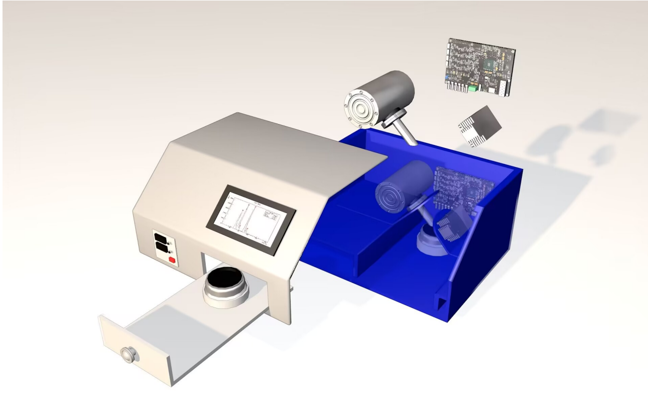

Fig. 1. (Color online) The physical structure diagram of the XRF system.

III. HARDWARE DESIGN OF THE PRE

The prototyping of the readout electronic (PRE) requirements for precision measurement differ from those of on-site rough measurement. Due to the expectation for fast and accurate measurement, the front-end electronics require high speed and low noise. Readout electronics for XRF are significant to produce, so it is necessary to design the prototypes first and validate the functionality of the design.

The PRE uses the FPGA to get highly reliable speed and low noise levels. For the PRE, two AD9248 [35] were used to realized 4 channels of detector signal readout. Figure 3 shows the block diagram and photograph of the PRE, which includes a filter circuit, the power management circuit, an ADC (Analog-to-Digital Converter) circuit, a field-programmable gate array (FPGA) circuit, the communication interface circuit, and the detector signal interface circuit. The PRE uses a Xilinx Kintex-7 FPGA for control and data transmission. The charge pulse signal generated by the detector is connected to the PRE via a LEMO connector or FPC connector. The charge signal is integrated and shaped in the filter circuit before being sent to the ADC circuit for digitization. The FPGA receives the data from the ADC circuit, processes and packages it, and transmits it to the host computer through a Gigabit Ethernet link. In addition, the PRE can receive control commands through the universal asynchronous receiver/transmitter (UART) interface or universal serial bus (USB) 3.0, and transmit parameter information to the host.

A. Filter Circuit

The filter circuit plays a crucial role in the system, with its primary function being to eliminate noise and unwanted frequency components from the input signal, thereby ensuring the stability and accuracy of the signal. Capacitors placed near the power supply voltage regulator chip are designed to filter out high-frequency noise and fluctuations in the power supply, ensuring the stable output of the current (DC) power and preventing power fluctuations from affecting the nor-

TABLE 1. X-ray Generator Parameters

Input Voltage	$\leq$ 50 kV	Focal Spot Size	$\leq$ 0.1 mm
Anode Current	$\leq$ 1 mA	Beryllium Window Thickness	200 μm
Filament Voltage	$\leq$ 2.2 V	Target Material	Ag(Silver)
Filament Current	$\leq$ 1.9 A	Operating State	Continuous Operation
Maximum Power	50 W	Stability	$\leq$ 0.4% within 4 hours

TABLE 2. XR100-CR Si-PIN Detector Parameters [36]

Type	Si-PIN	Cooling Method	Electro-cooling
Detector Area	25 mm^2	Measurement Range	1 $\sim$ 60 keV
Thickness	500 μm	Count Rate	50 kcps
Power Consumption	1.2 W	Full Width at Half Maximum (FWHM)[a]	140 eV @ 5.9 keV

[a] Obtained by the ^{55}Fe standard source

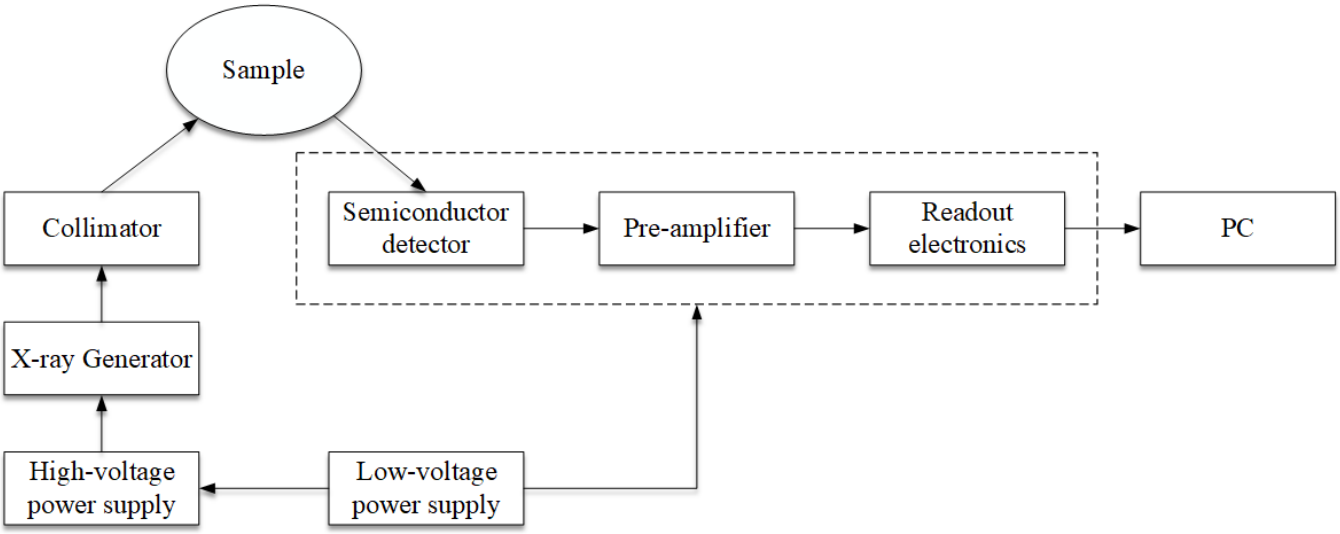

Fig. 2. The workflow diagram of the XRF System.

mal operation of amplifiers and other components. A filtering network is implemented at the input and output terminals of each operational amplifier. The input stage high-pass filter is formed by a combination of capacitors and resistors, creating a high-pass filter that eliminates the direct DC component or low-frequency noise from the input signal, allowing the operational amplifier to process only high-frequency alternating current (AC) signals. This design effectively prevents DC offset from affecting the stability of the amplifier's operation. The output stage low-pass filter is placed at the output terminal of the operational amplifier, used to suppress high-frequency noise and prevent interference signals from entering subsequent circuits or the data acquisition system.

B. Power supply circuit

To ensure the consistent operation of the PRE, a stable power supply is necessary. The circuit system is supported by an external 6V power supply to power the FPGA and other chips, meeting the power-up sequence requirements of the Xilinx FPGA. The power supply circuit is capable of provid-

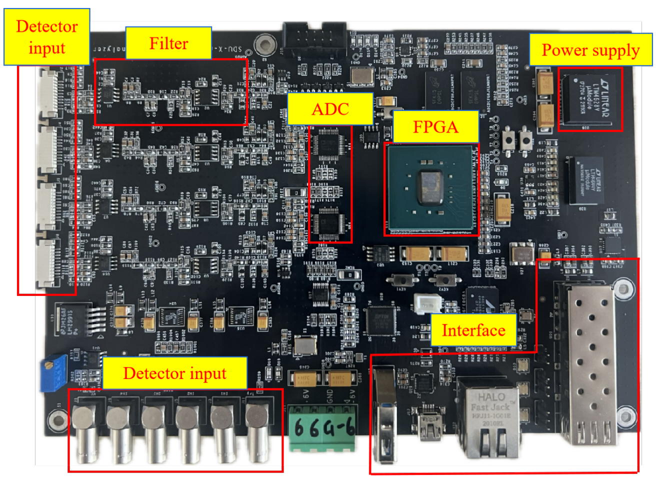

Fig. 3. (Color online) A Physical Layout of the XRF Prototype Readout Electronics.

ing stable voltage outputs of 1.8 V, 2.5 V, 1.5 V, and 3.3 V, meeting the operational requirements of different modules. By adjusting the components and feedback loops, the system can precisely maintain the stability of each voltage rail, preventing voltage fluctuations from affecting the system's operation.The power supply circuit utilizes the LTM4644 voltage regulator chip, which converts the input 6V voltage into the different required voltages for each module. Additionally, by adjusting the output voltage of each rail, the system ensures that all components receive the precise and appropriate voltage values.

C. ADC Circuit

The ADC circuit is centered around the AD9248 dual-channel 14-bit analog-to-digital converter, with its primary function being to convert the input analog signal into a digital signal, which is then output to an FPGA. To ensure the accuracy and stability of the ADC conversion, the circuit design covers multiple aspects, including power supply, analog input, reference voltage, digital interfaces, and signal conditioning. The ADC power section is supplied with +3.3V power, and filtering capacitors are used effectively to suppress high-frequency noise in the power supply, ensuring stable operation of the chip. The analog input channels are configured with a series of filtering components before the input signal to remove high-frequency noise and improve signal quality. The reference voltage is provided by the precision reference voltage source MCP1501T-10E, ensuring that the AD9248 has a stable voltage reference during the analog-to-digital conversion process, thereby enhancing conversion precision. The AD9248 outputs a 14-bit digital signal through a parallel interface, with the sampling rate controlled by a clock signal to ensure the reliability of data sampling. The control signals are managed by the FPGA or other controllers, allowing for flexible adjustment of the ADC's operational state. To further optimize signal quality, an anti-aliasing filter is added at the ADC input to reduce the impact of high-frequency noise and aliasing on sampling fidelity.

D. FPGA circuit

The FPGA used in this system is the Xilinx Kintex-7 XC7K70T-2FBG676I [37], which executes control and data transmission via an optical link. Figure 4 illustrates the FPGA-based architecture design. The process begins with the detector capturing the X-rays and converting them into current signals. These signals are then initially processed by the front-end electronics. The front-end circuit includes filters, which filter out noise. This ensures the signal stability and accuracy necessary for precise measurements.

Once processed, the analog signals are converted into digital signals by the AD9248, which are then sent to the FPGA for further digital signal processing. The FPGA uses high-frequency clock signals provided by an external crystal oscillator, performing tasks such as data preprocessing and packetization.

The processed data is ultimately transmitted to a computer for further analysis via a Gigabit Ethernet interface. The system's power module ensures that each functional unit receives stable voltage, thereby guaranteeing the reliability and efficiency of the entire system.

This design is particularly well-suited for applications requiring high-precision data acquisition and processing, ensuring both accuracy and robustness in complex measurement environments.

E. Interface circuit

The Si-PIN detector offers good energy resolution and a low detection threshold. For the PRE implementation, a LEMO connector or FPC connector is adopted for signal transmission. Additionally, to test the electronics performance, four standard LEMO connectors and four standard F-PC connectors can be used interchangeably to extract the four input signals from the Si-PIN detector for real-time monitoring.

A highly reliable communication interface connection is required between the PRE and the host computer. The PRE's configuration commands downstream and status parameters upstream are transmitted through a UART interface. The scientific data transfer interface is designed to use a small form-factor pluggable (SFP) connector. Data transmission to the host is carried out via Gigabit Ethernet, and for compatibility with different environments, a USB 3.0 interface is also provided.

IV. SOFTWARE DESIGN OF THE PRE

The algorithm section outlines the framework used for signal processing and elemental analysis within the system. The process begins by acquiring original signals from the detector, followed by a series of signal conditioning and processing steps aimed at noise rejection, peak identification, and concentration calculation of the target elements. Each step of the algorithm is carefully designed to address challenges such as signal noise, background interference, and X-ray attenuation, which can all impact the precision of the measurements. Specific methods employed in the signal processing include Moving Average Filtering (MAF) [38], Moving Window Deconvolution (MWD) [39–42], and background subtraction, all of which collectively enhance the system's accuracy.

A. FPGA Internal Algorithms

The signal amplitude and arrival time being critical parameters for physical studies. In particular, the amplitude directly reflects the energy information of the particle. During the signal acquisition process from the detector, the signal is first

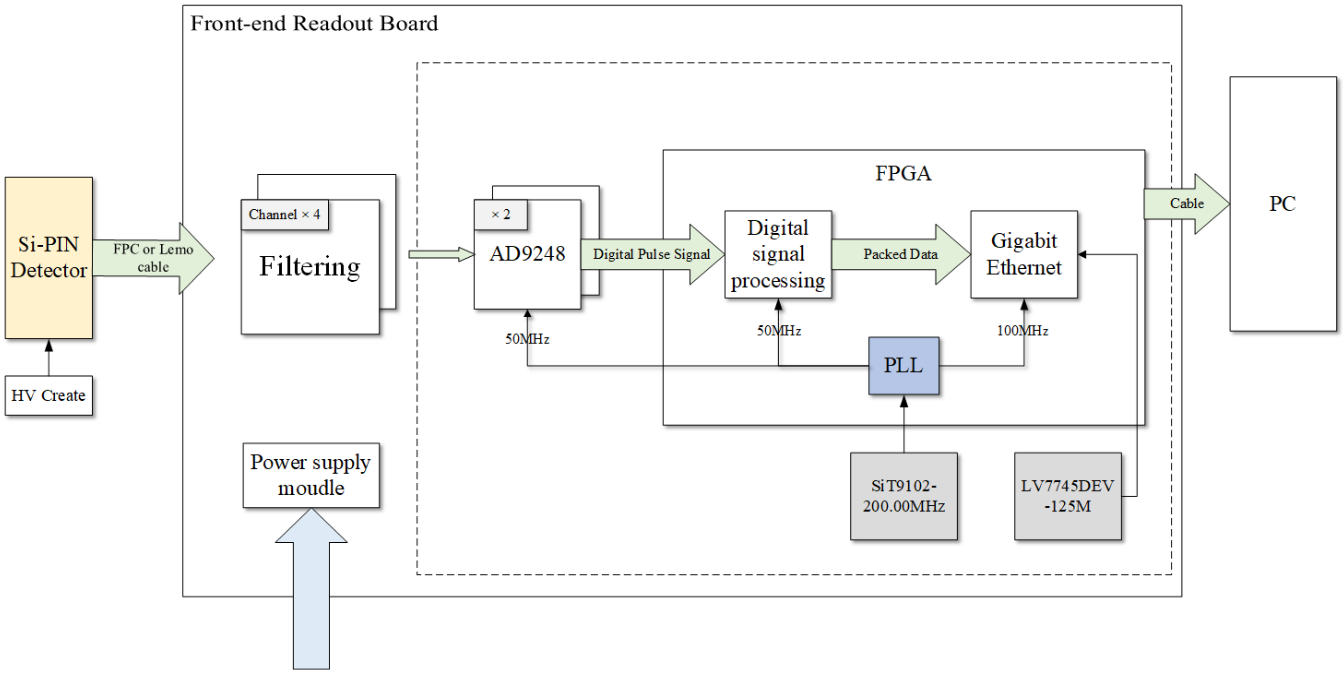

Fig. 4. (Color online) The block diagram of the XRF Prototype Readout Electronics.

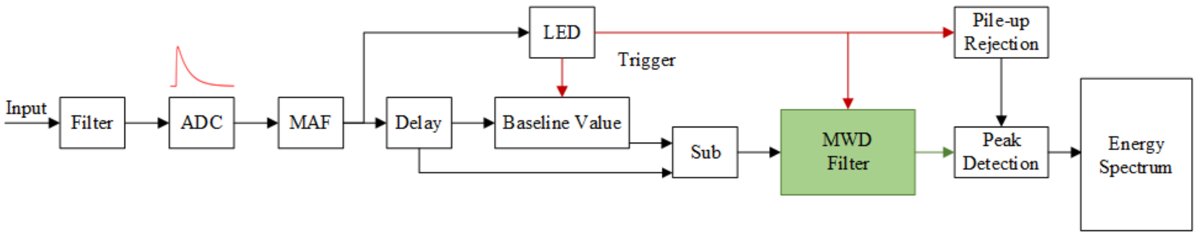

Fig. 5. (Color online) FPGA internal algorithm flow.

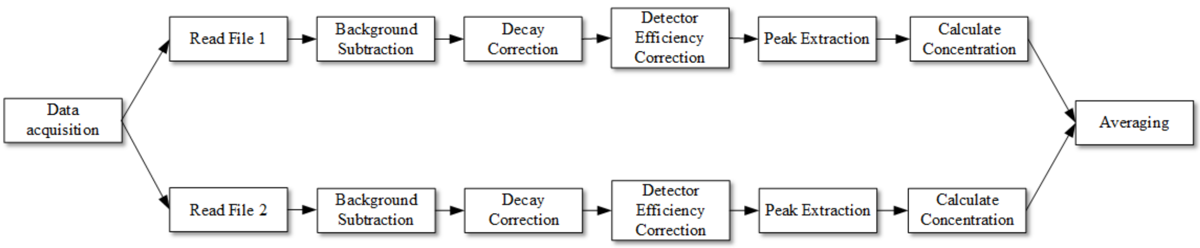

Fig. 6. (Color online) FPGA internal algorithm flow.

amplified by a charge-sensitive preamplifier and then sampled by an ADC. However, due to environmental background noise and hardware noise within the electronic system, the signal is inevitably affected during acquisition, which in turn impacts the energy resolution of the detector and reduces the measurement accuracy. Excessive noise may even cause the system to trigger falsely, generating invalid data. Therefore, filtering [43–45] must be applied to the signal before it is read out, in order to minimize the impact of noise, while preserving the signal characteristics and improving the signal-to-noise ratio (SNR) of the data.

Figure 5 illustrates the overall flow of the algorithm used in the system.To obtain the final energy spectrum, we use the Moving Average Filter (MAF) [38] algorithm. This algorithm smooths the signal waveform to filter out the influence of noise, while minimizing changes to the overall shape of the signal, ensuring the integrity of the signal's characteristics. Here, the leading-edge discrimination (LED) [38] method is employed as a time-triggering mechanism, providing support for subsequent data processing.

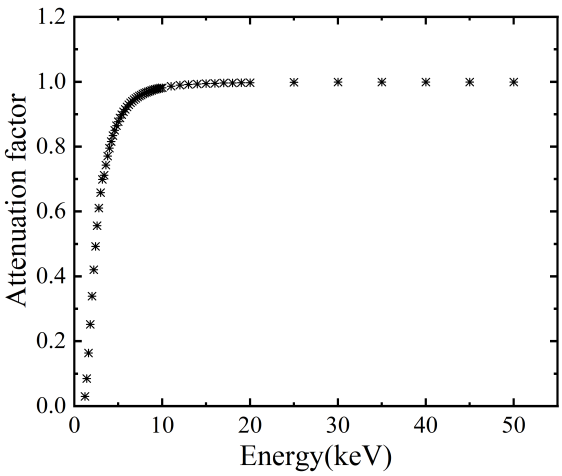

Fig. 7. X-ray attenuation efficiency curve in 10 mm air.

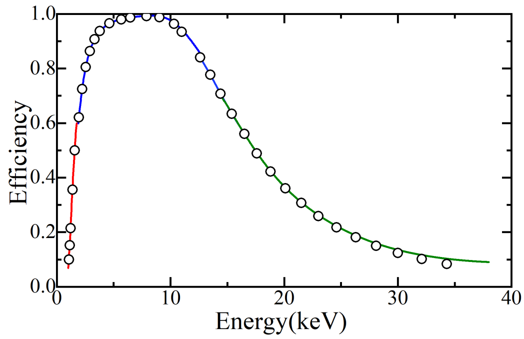

Fig. 8. (Color online) The detection efficiency of Si-PIN detector as a function of the energy. The line represents the fitted results, while the circles represent the raw data.

In the process of signal amplitude extraction, due to issues such as ballistic loss, noise, and signal pile-up in real-world systems, directly obtaining the maximum value may affect the accuracy of the signal amplitude, thereby reducing the energy resolution of the detector. To address this issue, this paper adopts the Moving Window Deconvolution (MWD) [39–42] trapezoidal shaping algorithm.

The MWD algorithm is a hardware-friendly and computationally efficient trapezoidal shaping method. It works by convolving the slowly decaying exponential signal, transforming the long tail of the signal into a rectangular pulse, where the pulse duration is equal to the width of the moving window. This algorithm achieves the trapezoidal shaping effect with minimal computational effort and significantly enhances system performance. Through this processing method, the amplitude of the signal can be extracted more accurately, thereby improving the energy resolution and reducing the impact of noise and pile-up effects on the signal.

B. Data Processing Algorithms

The main functions of the host computer include receiving and storing data processed by the FPGA, and displaying the system test results and waveforms in a visualized manner in real-time. The host software interface provides an intuitive view of the processed data and supports the real-time transmission of the results to a cloud platform, facilitating subsequent data analysis and processing.

Figure 6 presents the complete data processing flow, during the data acquisition process, two sets of data are recorded sequentially. Subsequently, the host computer begins to read the two sets of files along with several data processing parameters, including the characteristic X-ray energy table, the background from the silver element in the X-ray generator, the attenuation factor of X-rays in air, and the efficiency of the Si-PIN detector. To eliminate the impact of background interference, we collect the background signal under the same conditions as the actual test, but without placing the sample. The collected data is then subjected to Gaussian fitting for further processing. The fitted results will be subtracted from the subsequent data to achieve the correction.

The attenuation correction of X-rays in air is also considered in the current work, which allows the current device to be used in a non-vacuum environment. We simulated the proportion of X-rays passing through 10 mm air (distance between detector and sample) at different energies. The simulation covered X-ray energies ranging from 0.5 keV to 50 keV. Using Geant4 [46, 47] software, a sensitive detector with a square shape and a side length of 800 mm was set, with the material being air. X-rays were emitted at a 2π angle from a point 10 mm away from the air, and the number of X-rays remaining after passing through the 10 mm of air was recorded. The simulation results show the relationship between X-ray energy and the remaining X-ray proportions after passing through air, as depicted in Fig. 7. The x-axis represents the energy of the X-rays, while the y-axis shows the X-ray attenuation factor which is the penetration ratio remaining after passing through 10.0 mm of air, denoted as ϵ_0.

In addition, the detector efficiency is also corrected. Based on the detector data provided by Amptek [36], we performed a polynomial fit to model the efficiency of the Si-PIN detector. To simplify the fitting process, we fit the curve at the three segment endpoints. Therefore, we performed fitting for three different energy ranges: red line represents 0-1.8 keV, blue line represents 1.8-15 keV, and green line represents 15-40 keV. The results are presented in Fig. 8. At this stage, the detector efficiency is denoted as ϵ_1. The initial X-ray counts are denoted as y_0, and the actual X-ray counts y should be written as :

$$y = \frac{y_0}{\epsilon_0 \times \epsilon_1} \tag{1}$$

Peak shape identification was performed after reading the file parameters and correcting the counts. For each detected peak, a Gaussian function is used to fit the data, determining the peak's center position, shape, and height. The energy of

the characteristic peak is then compared with known X-ray data tables to identify the corresponding element. To obtain the element concentration, we calculate the peak area based on the fitted curve, using the left and right boundaries of the peak. The integral method of the histogram [48] is employed, and the background integral is subtracted. The concentration calculation process is shown in equation (2), where P represents the proportion of a specific element, A_i represents the intensity of the characteristic X-rays of specific elements. Through this process, the relative concentration of the element in the detected sample can be determined. In order to reduce systematic error, the outcomes from the obtained two files are averaged and presented as the final result.

$$P(A_i) = \frac{A_i}{\sum_i A_i} \tag{2}$$

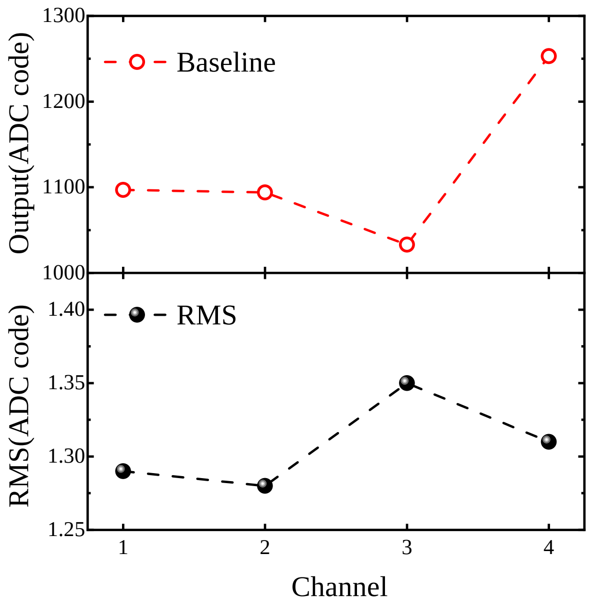

Fig. 9. (Color online) The baseline and noise test results of the readout electronics.

V. PERFORMANCE MEASUREMENTS

To explore whether the PRE design can meet the application requirements , a series of tests were performed to evaluate the functionality and performance of the proposed PRE design.In the laboratory tests, a signal generator (Tektronix AFG31000) generated a exponential signal, which fanned out to the PRE. The test results were analyzed to evaluate the performance of PRE and verify the reliability of the design. The pulse signal output simulated the charge signal generated by the Si-PIN detector.

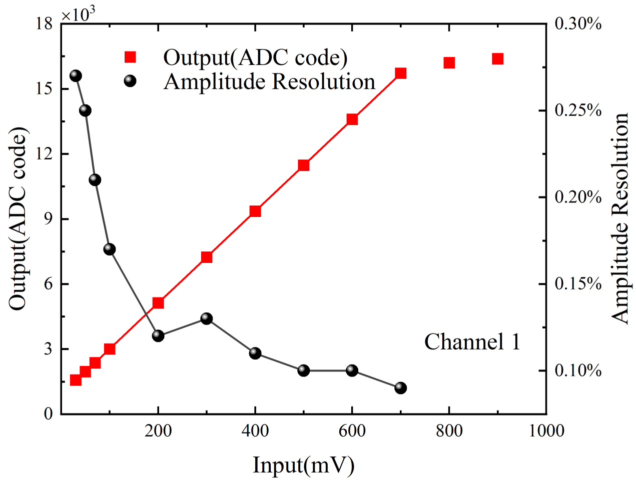

Fig. 10. (Color online) PRE's linear test results and Amplitude resolution test results.

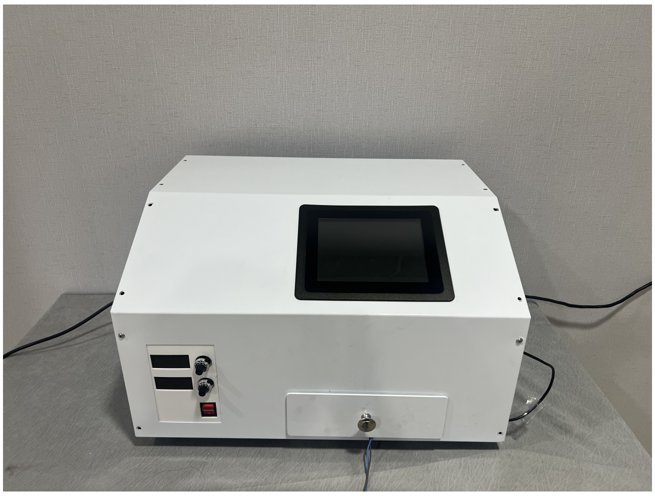

Fig. 11. (Color online) Experimental platform for joint test.

A. Baseline noise characterization

Noise characterization refers to the modeling of the random perturbations introduced during the signal transmission and processing, and is of great significance for interpreting experimental results, electronic model verification, and physical information extraction. Baseline noise testing is used to quantify system noise levels and evaluate the reliability of electronic data.

During the test, a baseline noise analysis of the 4 channels of the PRE was carried out. The trigger frequency is 10 kHz.This was aimed to simulate the state of the Si-PIN detector when it is in orbit during the transmission of uncompressed raw data. The level of noise was characterized through its Root Mean Square (RMS) value. Figure 9 illustrates the baseline data and corresponding RMS noise levels. The red circle represents the baseline level. The ADC codes range between 1250 and 1350. The black dots represent the

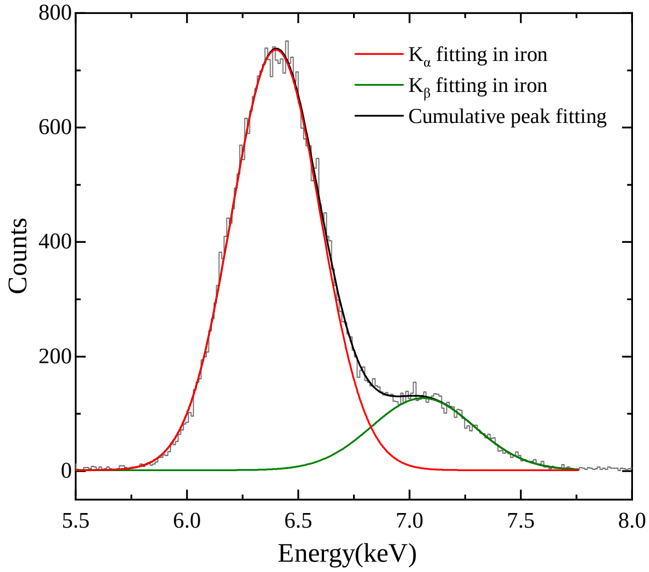

Fig. 12. (Color online) Obtained spectrum for the iron (Fe) content in an ore sample.

RMS noise of the electronic device. Analyze a dataset of 100,000 data points sampled from the baseline. From Fig. 9, it can be seen that the RMS noise of the PRE is below the 1.3 ADC code.

B. Channel linearity and Amplitude resolution test

To verify the channel linearity. A pulse signal generator is used to generate exponential voltage pulses, which are then sent to the PRE for data collection. Ideally, the relationship between the input and output of a readout electronics system is a linear function of positive proportion, whose slope represents the magnification of the readout system. In the present test, measurements are first taken at 30 mV, 50 mV, and 70 mV. For subsequent measurements, data is collected at increasing intervals, with each subsequent collection occurring every 100 mV increase in the voltage. After testing, the four channels exhibit similar characteristics. Figure 10 illustrates the linearity and amplitude resolution of the channel 1 as a example. From the figure, it can be seen that the linearity of the channel is good, and the slope is approximately 21.

Amplitude resolution indicates the electronics system's ability to resolve different input signal amplitudes and equivalently characterizes the energy resolution for the system. However, the K_α andK_β peaks of certain elements or the peaks of elements with similar proton numbers may overlap, complicating the accurate identification and differentiation of these elements. To overcome these challenges, it is essential for the readout system to have a high energy resolution. Figure 10 shows the amplitude resolution of channel 1 in the PRE at different input amplitudes. After 200 mV, the amplitude resolution is 0.15%. The other three channels also exhibit similar linearities and resolutions.

C. Joint test with Si-PIN

To verify the performance of the XRF design, conducting a joint test was necessary. The experimental platform was built as shown in Fig. 11. With just a single click on the user interface to initiate the measurement, the system begins the testing process. The testing duration was set to the standard 3 minutes. This streamlined process not only saves time but also enhances the overall ease of use, enabling rapid, real-time analysis without the complexity of traditional methods. The test system included the PRE, a Si-PIN, a low-noise digital power supply and a host computer. During the test, a piece of iron ore was used, We use an X-ray generator voltage of 15 kV and a current of 0.02 mA to irradiate the iron ore sample with X-rays.

Figure 12 shows the energy spectrum obtained under these conditions. The red and green curves correspond to the fitted characteristic peaks of iron (Fe), while the black curve represents the overall fit of the entire peak shape. From the figure, it is evident that the two characteristic peaks of iron are distinctly resolved, demonstrating the system's ability to effectively differentiate closely spaced energy levels in the lower energy range. The energy resolution of the 6.4 keV characteristic peak of iron is 7.35%.

In the test, we also obtained the iron content in the iron ore sample, yielding a result of 41% while the chemical method is 49%. This result indicates that the current XRF method achieves results close to those of chemical methods while offering fast and convenient measurement. This presents that the XRF system function is fully operational and meets the expected goals, confirming its effectiveness and reliability for elemental analysis.

VI. SUMMARY

In this paper, an XRF system including a Si-PIN detector, PRE, and software algorithm is designed. The PRE mainly consists of the power management circuit, an ADC circuit, a FPGA circuit, the communication interface circuit, and the detector signal interface circuit. The tests performed indicate that the PRE system performed well. The algorithm mainly includes the internal FPGA algorithm and the data processing algorithm on the host computer, working together to achieve qualitative and quantitative analysis results. The joint test shows results similar to those of chemical method. In the current work, an XRF system has been designed that allows the detector to be used in the air and enables online data transmission to the cloud platform, making it suitable for non-destructive measurement in complex environments such as industrial production lines and scientific research. It is worth noting that the current algorithm does not account for the correction of matrix effects. With the addition of this correction in future work, the accuracy of the system is expected to improve further.

[1] W.C. Röntgen, On a New Kind of Rays. Nature 274-276, **56**, 1473 (1895). doi: 10.1038/053274b0

[2] A. Ben-Yehuda, O. Sefi, Y. Klein et al., High-resolution computed tomography with scattered X-ray radiation and a single pixel detector. Commun. Eng. **3**, 39 (2024). doi:10.1038/s44172-024-00184-6

[3] X.Y. Ou, X. Chen et al., Recent Development in X-Ray Imaging Technology: Future and Challenges. Res. **9892152** (2021). doi:10.34133/2021/9892152

[4] M. Eckert, Max von Laue and the discovery of X-ray diffraction in 1912. Ann. Phys. 524, **5**, A83–A85 (2012). doi:10.1002/andp.201200724

[5] J.M. Thomas, The birth of X-ray crystallography. Nature 186–187, **491**, (2012). doi:10.1038/491186a

[6] H.G.J. Moseley, The high-frequency spectra of the elements. The London, Edinburgh, and Dublin Philosophical Magazine and Journal of Science **26(156)**, 1024–1034 (1913). doi:10.1080/14786441308635052

[7] D. COSTER, G. HEVESY, On the Missing Element of Atomic Number 72. Nature **111**, 79 (1923). doi:10.1038/111079a0

[8] D. COSTER, G. HEVESY, On the New Element Hafnium. Nature **111**, 252 (1923). doi:10.1038/111252a0

[9] R. Glocker and H. Schreiber, Quantitative Roentgen Spectrum Analysis by Means of Cold Excitation of the Spectrum. Ann.Phys. **390**, 1089-1102 (1928). doi:10.1002/andp.19283900805

[10] R.G. Egdell, E. Bruton, Henry Moseley, X-ray spectroscopy and the periodic table, Phil. Trans. R. Soc. A. **378** (2020). doi:10.1098/rsta.2019.0302

[11] Y.P. Liu, L. Yao, B.J. Wang et al. Silicon PIN photodiode applied to acquire high-frequency sampling XAFS spectra. Nucl. Sci. Tech. **33**, 91 (2022). doi:10.1007/s41365-022-01066-2

[12] H. Friedman, L.S. Birks, A Geiger counter spectrometer for X-ray fluorescence analysis. The Review of scientific instruments 19 **5**, 323-30 (1948). doi:10.1063/1.1741258

[13] R. He, X.Y. Niu, Y. Wang et al. Advances in nuclear detection and readout techniques, Nucl. Sci. Tech. **34**, 205 (2023). doi:10.1007/s41365-023-01359-0

[14] J.J. Thompson, R.A. Horowitz, R.L. Sappington, An evaluation of ED-XRF sourcing of vitrophyre artifacts and toolstone in North central Idaho, Journal of Archaeological Science: Reports, **56**, 104535 (2024). doi:10.1016/j.jasrep.2024.104535

[15] M.T. Yang, D.P. Ren, Practical X-ray Spectral Analysis. Atomic Energy Press. (2008).

[16] E.P, Bertin, Principles and Practice of X-Ray Spectrometric Analysis. Sec. ed, New York, (1975).

[17] L.Q. Ge and F.Li, Review of in situ X-ray fluorescence analysis technology in China. X-Ray Spectrometry, **49(4)**, 458-470 (2019). doi:10.1002/xrs.3135

[18] B.G. Feng, F. Tao, Y.M. Yang et al. X-ray fluorescence microtomography based on polycapillary-focused X-rays from laboratory source. Nucl. Sci. Tech. **29**, 85 (2018). doi:10.1007/s41365-018-0417-x

[19] X.Y. Lan, D.X. Liang and C.W. Mao. Scan system for arbitrary-shaped samples at the synchrotron radiation facility. Nucl. Sci. Tech. **28**, 60 (2017). doi:10.1007/s41365-017-0210-2

[20] R.Y. Lu, Q. Gao, S.Q. Gu et al. Data-collection system for high-throughput X-ray absorption fine structure measurements. Nucl. Sci. Tech. **27**, 82 (2016). doi:10.1007/s41365-016-0084-8

[21] S.C. Zhou, T.Z. Xie et al. A total content X- RAY fluorescence method for copper prospecting. Nucl. Sci. Tech. **3(3)**, 191-195 (1992). doi:www.nst.sinap.ac.cn/article/id/5881?lang=en

[22] M.A. Phedorin, E.L. Goldberg, Prediction of absolute concentrations of elements from SR XRF scan measurements of natural wet sediments, Nucl. Instrum. Methods Phys. Res. A **543** 274-279 (2005). doi:10.1016/j.nima.2005.01.240

[23] S.B. Huang, U. Nilsson, S. Mattsson et al. Non-destructive measurements of lead and barium in archaeological bone samples using XRF. Nucl. Sci. Tech. **2(1)**, 48-52 (1991). doi:www.nst.sinap.ac.cn/article/id/5941?lang=en

[24] V.V. Bazhanova, L.F. Guljaeva, S.E. Krasilnikov, V.S. Titova, A.D. Shaporenko, Y. Shulga, Using XRF SR for the study of changes in elemental composition of healthy and pathological tissues of human organism, Nucl. Instrum. Methods Phys. Res. A **575** 206-209 (2007). doi:10.1016/j.nima.2007.01.069

[25] F. Adrian, J.Kamil, Portable X-ray fluorescence (pXRF) as a powerful and trending analytical tool for in situ food samples analysis: A comprehensive review of application - State of the art, Trends in Analytical Chemistry, **166**, 117165 (1992). doi:10.1016/j.trac.2023.117165

[26] A. Harth, X-ray fluorescence (XRF) on painted heritage objects: a review using topic modeling. Herit Sci, **12** 17 (2024). doi:10.1186/s40494-024-01135-2

[27] Y.X. Zhang, X.P. Wang, J.F. Qin et al. Matrix absorption correction of medium thick targets in XRF. Nucl. Sci. Tech. **4(2)**, 120-124 (1993). doi:www.nst.sinap.ac.cn/article/id/5818?lang=en

[28] P.Q. Duan, H.L. Bao, J. Li et al. In-situ high-energy-resolution X-ray absorption spectroscopy for UO2 oxidation at SSRF. Nucl. Sci. Tech. **28**, 2 (2017). doi:10.1007/s41365-016-0155-x

[29] C. Liu, S.Y. Wang, R.A. Bark et al. Evidence for Octupole Correlations in Multiple Chiral Doublet Bands. Phys. Rev. Lett. **116**, 112501 (2016). doi:10.1103/PhysRevLett.116.112501

[30] C. Liu, S.Y. Wang, R.A. Bark et al. New candidate chiral nucleus in the A $\approx$ 80 mass region ^{82}Br. Phys. Rev. C. **833**, 137287 (2022). doi:10.1103/PhysRevC.100.054309

[31] W.Z. Xu, S.Y. Wang, C.Liu. et al. Interplay between nuclear chiral and reflection symmetry breakings revealed by the lifetime measurements in ^{76}Br. Phys. Lett. B. **116**, 112501 (2016). doi:10.1103/PhysRevLett.116.112501

[32] R.J. Guo, S.Y. Wang, C. Liu et al. Evidence for Chiral Wobbler in Nuclei. Phys. Rev. Lett. **132**, 092501 (2024). doi:10.1103/PhysRevLett.132.092501

[33] H.B. Yang, Z.G. Gan, Y.J. Li et al. Discovery of New Isotopes ^{160}Os and ^{156}W: Revealing Enhanced Stability of the N=82 Shell Closure on the Neutron-Deficient Side. Phys. Rev. Lett. **132(7)**, 072502 (2024). doi: 10.1103/PhysRevLett.132.072502

[34] Y.L. Liu, Q.X. Zhang, J. Zhang et al. Quantitative energy-dispersive X-ray fluorescence analysis for unknown samples using full-spectrum least-squares regression. Nucl. Sci. Tech. **30**, 52 (2019). doi:10.1007/s41365-019-0564-8

[35] AD9248 14-Bit, 40 MSPS Dual Analog-to-Digital Converter. https://www.analog.com/media/en/technical-documentation/data-sheets/ADW12001

[36] X-123 SiPIN Si-PIN X-Ray Detector. https://www.amptek.cn

[37] Xilinx Corporation, 7 Series FPGAs Data Sheet: Overview. https://docs.xilinx.com

[38] T. Liu, H.S.Song, Y.H. Yu et al. Toward real-time digital pulse process algorithms for CsI(Tl) detector array at external target facility in HIRFL-CSR. Nucl. Sci. Tech. **34**,131 (2023).

doi:10.1007/s41365-023-01272-6

[39] A. Georgiev and W. Gast, Digital pulse processing in high resolution, high throughput, gamma-ray spectroscopy, IEEE Trans. on Nucl. Sci. **40**, 770-779 (1993). doi:10.1109/23.256659

[40] J. Stein, F. Scheuer, W. Gast, A. Georgiev, X-ray detectors with digitized preamplifiers, Nucl. Instrum. Methods Phys. Res. B, **4113**, 141-145 (1996). doi:10.1016/0168-583X(95)01417-99

[41] J. Kamleitner, S. Coda, S. Gnesin, Ph. Marmillod, Comparative analysis of digital pulse processing methods at high count rates, Nucl. Instrum. Methods Phys. Res. A **736**, 88-98 (2014). doi:10.1016/j.nima.2013.10.023

[42] M.Bendel, R. Gernhäuser, W.F. Henning et al. RPID — A new digital particle identification algorithm for CsI(Tl) scintillators. Eur. Phys. J. A **49**, 69 (2013). doi:10.1140/epja/i2013-13069-8

[43] M. Wang, J.B. Zhou, X.P. Ouyang et al. Gaussian shaper for nuclear pulses based on multilevel cascade convolution. Nucl. Sci. Tech. **33**, 160 (2022). doi:10.1007/s41365-022-01145-4

[44] X.Y. Wang, J.B. Zhou, M. Wang et al. Signal modeling and impulse response shaping for semiconductor detectors. Nucl. Sci. Tech. **33**, 46 (2022). doi:10.1007/s41365-022-01027-9

[45] J. Liu, J. Yang, G.Q. Zeng et al. Implementation of a cusp-like for real-time digital pulse shaper in nuclear spectrometry. Nucl. Sci. Tech. **28**, 103 (2017). doi:10.1007/s41365-017-0248-1

[46] W.K. Chen, L.Q. Hu, G.Q. Zhong et al. Study on the gamma rays and neutrons energy response optimization of a scintillating fiber detector for EAST with Geant4. Nucl. Sci. Tech. **34**, 134 (2023). doi:10.1007/s41365-023-01290-4

[47] Z. He, N. Huang, P. Wang et al. Spatial resolution and image processing for pinhole camera-based X-ray fluorescence imaging: a simulation study. Nucl. Sci. Tech. **33**, 64 (2022). doi:10.1007/s41365-022-01036-8

[48] L. Szentmiklósi, Fitting special peak shapes of prompt gamma spectra, J. Radioanal Nucl. Chem.**315**, 663–670 (2018). doi:10.1007/s10967-017-5589-z